UC Riverside

UCR Honors Capstones 2019-2020

Title

Influence of Magnetic Fields in Gold Nanoparticles on the Generation of Microbubbles

Permalink

https://escholarship.org/uc/item/0wg9m4zx

Author

Ho, Benjamin

Publication Date

2021-01-11

Data Availability

The data associated with this publication are within the manuscript.

By

A capstone project submitted for
Graduation with University Honors

University Honors
University of California, Riverside

APPROVED

_____
Dr.
Department of

_____
Dr. Richard Cardullo, Howard H Hays Jr. Chair, University Honors

Abstract

Acknowledgements

I give thanks to the Vuong lab for giving me the environment and opportunity to explore the research world. I give thanks to Dr. Vuong for her guidance and encouragement, and I give thanks to Gaurav Ahuja for mentoring and pushing me through this project. I give thanks to Dhamar and the others who worked on this project before me.

Table of Contents

1. Introduction

Mechanisms of bubble formation and growth remain largely undefined. The science behind their formation, growth, shape changing, and rupture behavior continues to be studied. Macroscopic bubble behavior intrigues researchers in many fields of engineering, geophysics, and biophysics (Mandracchia *et al.*, 2019). Researchers propose using metal nanoparticles and vapor generation for renewable energy and desalination (Liang *et* al, 2019, Wang *et* al, 2019). Microbubbles have been used to precisely deliver drugs with single laser pulses or ultrasound waves for the drug release (Anderson *et al.*, 2010, Chen & Hwang, 2013). There are other biomedical applications, including cancer treatments involving the light-induced nanobubbles with plasmonic nanoparticles (citation attached).

Until recently, it was assumed that bubbles form as a result of the strongly-localized heating at metal nanoparticles as a result of plasmons or surface charge oscillations. Light is an electromagnetic wave that interacts with free electrons on the nanosized gold spheres. When the light-electron interaction is strong, the resonance is associated with plasmons. In this interpretation, the gold nanoparticles absorb electromagnetic energy from pulsed lasers. When the electrons slow down, the their energy is transferred to the gold bulk as well as the solvent surrounding the nanoparticle, which heats up (Kim *et al.*, 2013). This localized heating can lead to the generation of nanobubbles near the nanoparticle surface, and these small vapor nanobubbles are hypothesized to converge together to form vapor microbubbles (Lukianova-Hleb *et al.*, 2010, Wang *et al.*, 2017). Once the vapor bubble is formed, dissolved gas molecules diffuse into the bubble to stabilize it. Localized heating from the nanoparticle continues to contribute to the microbubble growth, yet at a far lesser degree than during the bubble's formation (Wang *et al.*, 2017). Using a femtosecond to a nanosecond-pulsed laser, one study

found that the localized heating caused bubble generation surrounding the nanoparticle (Metwally *et al.*, 2015).

More recent studies reveal nuanced details related to and contradicting this model. For example, the vapor bubble does not depend on the power absorbed but the relative illumination rate, and continuous wave illumination, rather than pulsed wave illumination, produces microbubbles. One study cited that pulsed lasers may produce destructive shockwaves that cause shorter bubble lifespans. This study observed longer lifespans in larger bubbles due to continuous wave illumination, attributing the trend to the greater volume of dissolved gas (Baffou *et al*., 2014). Another study discovered that metal nanoparticles that absorb light over a wide range can be a nucleation site for nanobubbles under normal sunlight, similar to continuous wave illumination (Neumann *et al.*, 2013). Cavitation, when bubbles form via pressure waves rather than thermal effects, may explain why some researchers observe bubbles with pulsed lasers when others do not.

The movement of bubbles in a solution is dependent on the gas that fills the bubble. In a nanoparticle solution, bubbles may react differently to a magnetic field, and bubbles containing diamagnetic gases may follow similar trends when subjected to a magnetic field. For example, oxygen bubbles generated in an electrolytic solution and subjected to a magnetic field had their motion dictated by the orientation of the magnets (Wang *et al*., 2016).

In my research project, we aim to draw larger statistical analyses to observe the movement of microbubbles We use a genetic algorithm programmed in Matlab. Genetic algorithms are useful for mass processing data requiring optimization of multiple parameters. Genetic algorithms are comprised of seven basic steps: (i) Population Generation, (ii) Crossover, (iii) Mutation, (iv) Genotype-Phenotype matching, (v) Fitness, (vi) Selection, and (vii)

Termination. Each step requires randomization and a lack of bias to prevent false optimization (Kramer, 2017).

This paper examines three conditions surrounding microbubbles. First, we observe how microbubble generation and growth is affected by the gold nanoparticle solution as opposed to water, each under neutral conditions and a magnetic field. Second, we record the motion of carbon dioxide microbubbles when subjected to a magnetic field. Third, we employ a genetic algorithm to identify and quantify microbubble position and radii, and we evaluate the effectiveness of such approach.

2. Materials and Methods

2.1 Slide Preparation

To prepare for microscope observations, well slides undergo the same sample preparation. The slide is placed into a beaker filled with ethanol solution, and the beaker is sonicated for 30 min. The slide is dried with a Kimwipe, and the dimple slide is cleaned first with acetone solution, then with methanol solution, then airbrushed to remove any contaminates.

2.2 Materials

This experiment is observed with two different solutions, deionized water and a gold nanoparticle solution. The nanoparticle fluids contain 60nm polyvinylpyrrolidone (PVP)-coated gold nanospheres with a concentration of 0.05mg/mL in water (NanoComposix). The PVP is a surfactant that covers the gold nanoparticles and prevents coagulation. Samples are stored at 4°C and shaken for 30 seconds before each use. 4 drops of solution are dispensed into each well slide to generate the sample. Samples are separated into three sets: ambient air, degassed, and dissolved carbon dioxide. Both degassed and dissolved carbon dioxide samples require initial degassing of the solution. Once the drops are placed onto the well slide, the slide is moved into a vacuum chamber and degassed for 5 min. 16g of carbon dioxide were injected into the chamber after degassing to dissolve the pure gas into the solution. A coverslip is slid over the well, and a Kimwipe is used to remove any excess fluid.

2.3 Capture Equipment

Prepared samples are placed beneath a microscope camera on a motorized stage and illuminated by an LED lamp to provide continuous wave illumination. The imaging system is an inverted microscope with a 5X microscope infinity-corrected objective and a 20-cm camera lens.

Once a bubble is located, a Matlab program moves the motorized stage and takes pictures to create a 5x5 grid of images, an area of 5.1mm by 6.7mm, over 4.4 min per iteration. To track the growth and motion of the bubbles, the program is run with 7 iterations for a total of 30.8 minutes per sample.

For magnetic samples, two horseshoe magnets with a total constant magnetic field strength of 190mT are placed level with the sample slide. The magnetic field traveled from bottom to top relative to the images captured by the camera.

3. Results and Discussion

3.1 Bubble radii and volume

The images captured by the microscope camera were processed by the genetic algorithm to locate the center coordinates and determine the radii of the bubbles for each iteration. The initial radii ranged from 40-400μm across all samples, and the final radii ranged from 100-1100μm across all samples. After examining the pressure in the vacuum chamber caused by the 16g carbon dioxide cartridges, we determine that the larger bubble formations are likely due to effervescence instead of bubble nucleation on the gold nanoparticles.

Despite effervescence, the initial radii of the bubbles did not depend on the solution used. Water and gold solution produced bubbles with similar initial radii. The determining factor of initial radius is the number of bubbles present in the sample. Single bubble samples tended to have larger initial radii than samples with multiple bubbles (Figure 1).
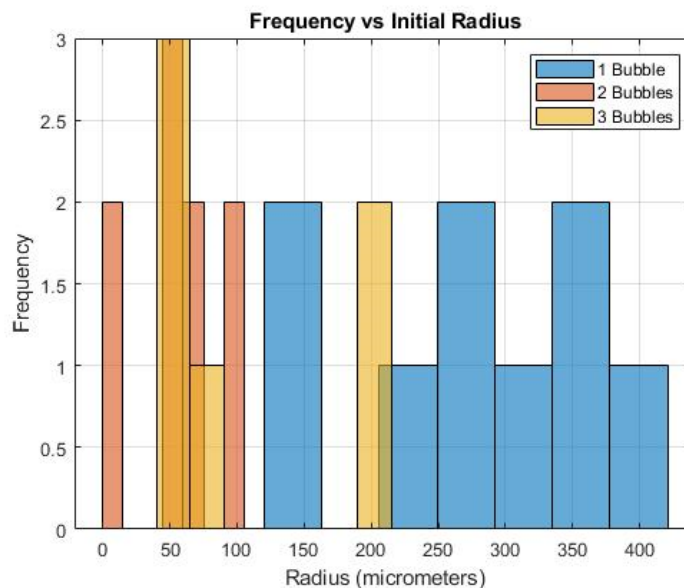
Figure 1. Histogram of the frequency that bubbles of certain radii form in the first iteration. Most samples possessed only a single bubble. Samples with more than one bubble appeared less often and had smaller initial radii on average than single bubble samples.

Gold solution samples had a larger number of bubbles per sample on average than water samples. Water samples had an average of 1.3 bubbles per sample, while gold solution samples had an average of 2.2 bubbles per sample. The presence of a magnetic field did not significantly alter the number of bubbles formed.

To calculate volume, bubbles are assumed to be spherical for each iteration. This calculation likely overestimates bubble growth, since we expect that the bubbles are flattened vertically against the coverslip. With a spherical approximation, the volume growth rate is found to be greater for bubbles with larger initial radii than for bubbles with small initial radii on average (Table 1). This is attributed to the greater surface area present in bubbles with larger volume, thereby facilitating greater gas exchange with the dissolved gas in the surrounding solution. The growth trend remains for most samples regardless of the number of bubbles,

although a few exceptions were observed. Since bubbles in the samples with multiple bubbles present were smaller on average, their growth rates were shown to be less on average as well. When this trend is related to the previous observation regarding the number of bubbles in water and gold solutions, we observe that the bubbles in gold solution grow at a slower rate than bubbles in water. Further testing is required to solidify such a claim. One reason for the lower rate of measured bubble formation may be related to the presence of PVP in the nanoparticle solution, which is expected to reduce surface tension. This may be a result of bubbles forming around nanoparticles that are too small for the imaging system, which can, at best with a 5X objective, image with 70-micron resolution.

Table 1

Volume growth rate for bubbles compared to initial radii for bubbles. Outliers are italicized.

Solution and Conditions	Initial Radius (µm)	Volume Growth Rate (µm³/min)
Gold Solution	50.26703	$1.35*10^5$
Gold Solution	69.84208	$3.39*10^5$
Gold Solution	94.41763	$5.77*10^5$
Gold Solution	136.96	$9.75*10^5$
Water	*147.0839*	*$8.76*10^5$*
Gold Solution	236.5915	$2.12*10^6$
Magnetic Gold	*256.80*	*$8.85*10^6$*
Gold Solution	295.9297	$7.78*10^6$
Water	341.5346	$1.14*10^7$
Magnetic Gold	368.7812	$1.35*10^7$
Gold Solution	414.4894	$3.13*10^7$

3.2 Magnetic field induced bubble motion

The center position of each bubble was calculated by the genetic algorithm and recorded for each iteration of a sample. The location of the bubble is given by pixel coordinates in the picture, starting from the top left corner of the image, as the top left image is the first picture

captured by the microscope camera. The stage moves the sample so that pictures are taken top to bottom, moving left to right (Figure 2).

In the samples with a magnetic field, bubbles either drift slowly in one direction (Figure 3) or in random directions (Figure 4). The most common direction of drift is towards the bottom right, in the direction opposite to the translation stages. However, this observation occurs statistically. The stage movement is dictated by a program to maintain consistent acceleration and velocity. The translation stage moves in smaller increments and with slower speeds in one vertical direction than the other. We cannot yet make any conclusion in regards to the nanobubble drift, since the stage may have an effect.
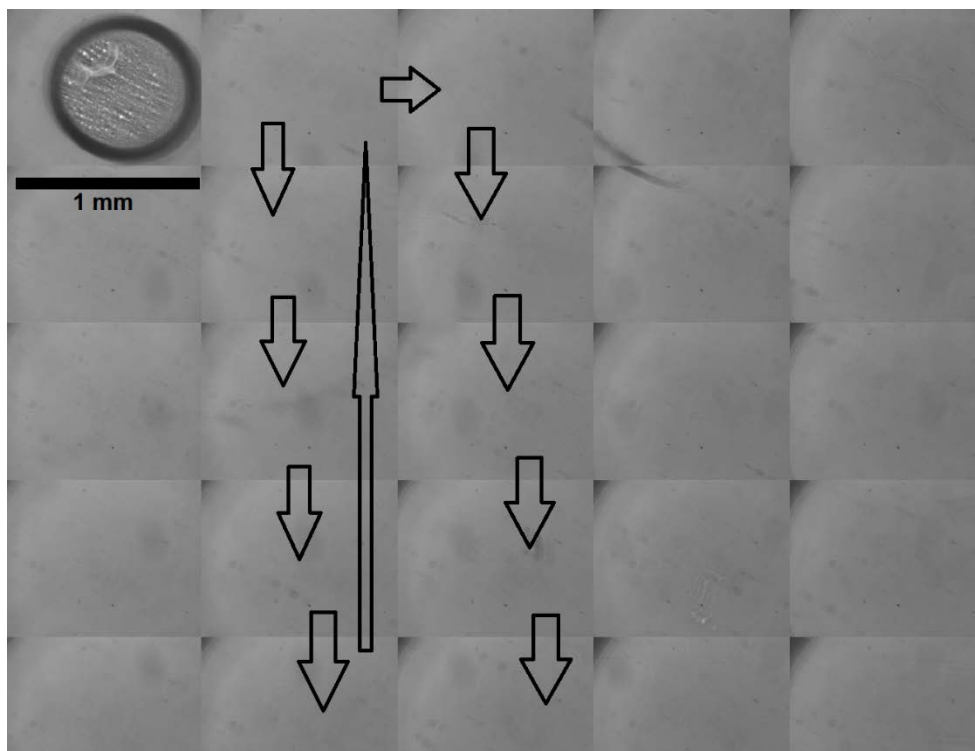
Figure 2. Order in which the microscope camera takes pictures as the motorized stage moves.
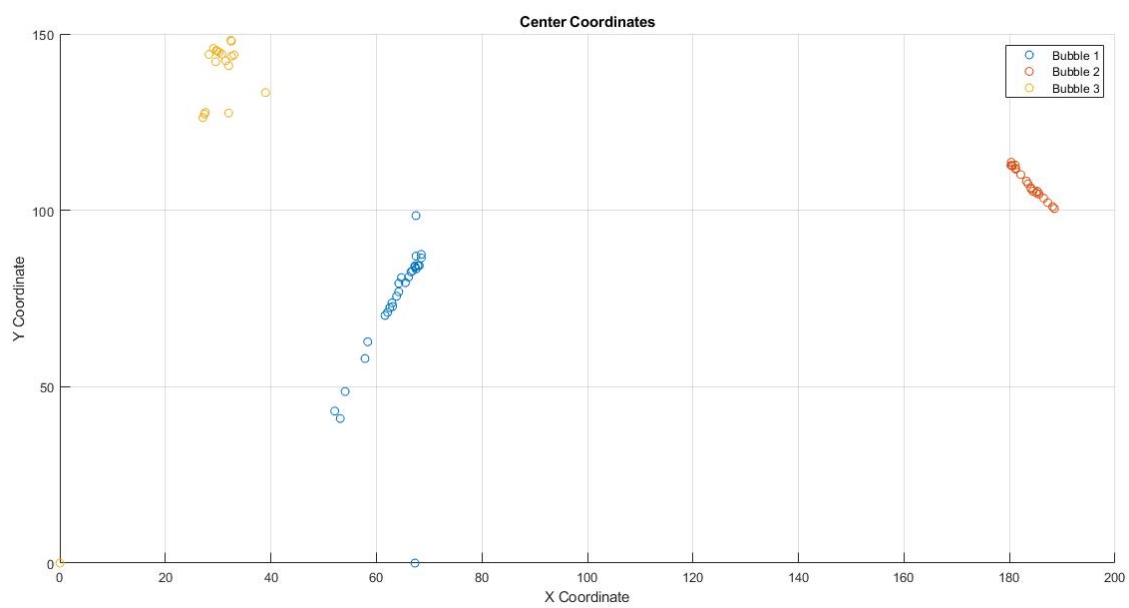

Figure 3. Drifting tendency of bubbles in gold solution. Movement of bubbles appear random.
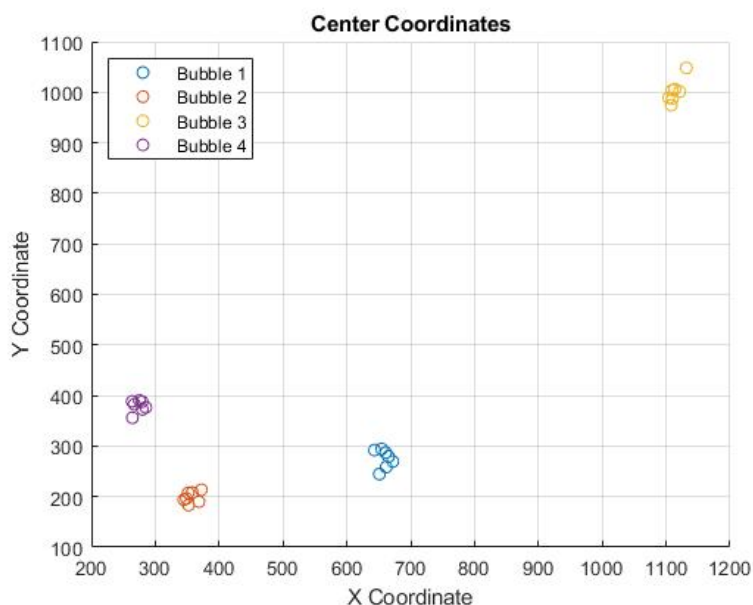
Figure 4. The pixel coordinates of a non-magnetic 4-bubble sample. Bubbles in non-magnetic samples typically did not exceed 40 pixels of distance between the initial and final positions.

The 190mT magnetic field was applied from the bottom to top of the sample relative to the images captured. The first sample set had carbon dioxide gas dissolved into the gold solution after the sample was degassed. The second sample set had air dissolved into the gold solution without degassing. The most significant motion of bubbles was observed in the air sample set, with both bubbles drifting vertically in the direction of the magnetic field by 90 pixels (Figure 5). Although the air samples contained the largest consistent motion, this result was not observed throughout the entire set. Random motion within the typical range of 40 pixels was most common in both air and carbon dioxide samples.

The carbon dioxide sample set experienced a similar vertical motion relating to the direction of the magnetic field (Figure 6). The bubbles drifted downward towards the positive end of the magnetic field. It should be noted that the carbon dioxide bubbles expanded in this downward direction, thereby shifting their center in the same direction.
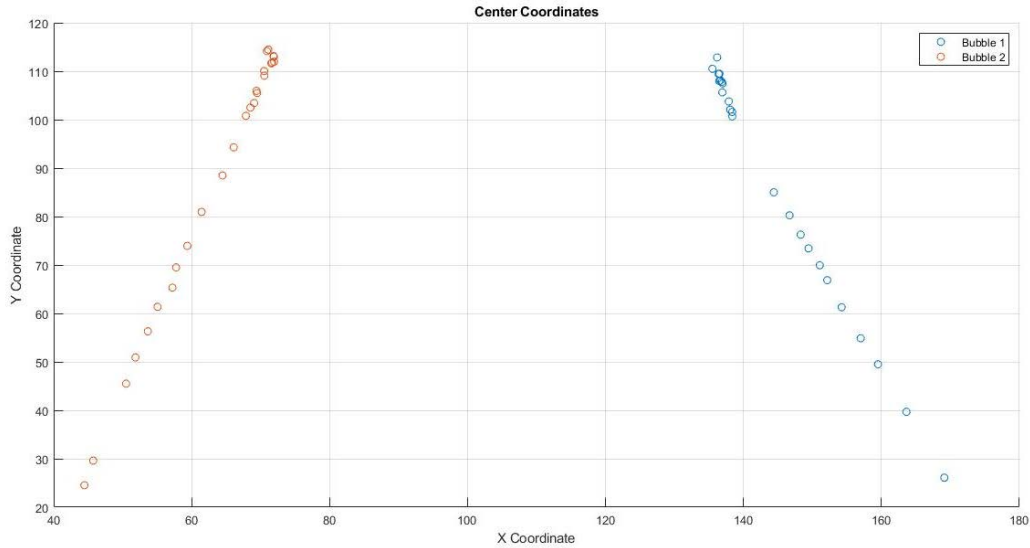
12

Figure 5. Center coordinates of two air bubbles in gold solution. Although their horizontal motion was opposite each other, the bubbles in this magnetic sample drifted at very similar rates, suggesting an influence in the setup.

There are several possible reasons for the lack of influence with the magnetic field in these

preliminary measurements. Firstly, the magnification of the microscope is not very high, so that

the magnetic field may have an effect but with nanobubbles that are smaller than the

microbubbles that are currently imaged. Secondly, the strength of the light source is also very
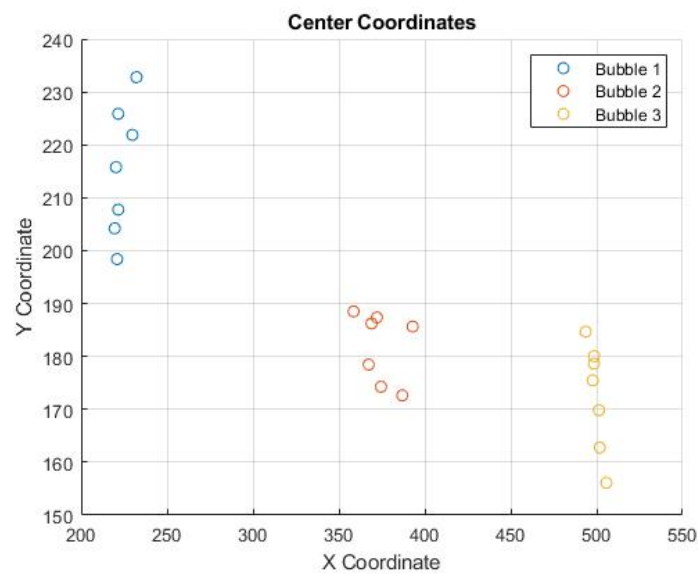
low so that the influence of plasmons, which give rise to nanoparticle magnetic dipole effects,

are small. The plasmonic resonance of the 60-nm gold nanoparticles occurs at 550nm where the

LED emission is low. While resonance has been demonstrated with sunlight according to

Neumann, the strength of the LED lamp was likely not enough to induce a similar effect.
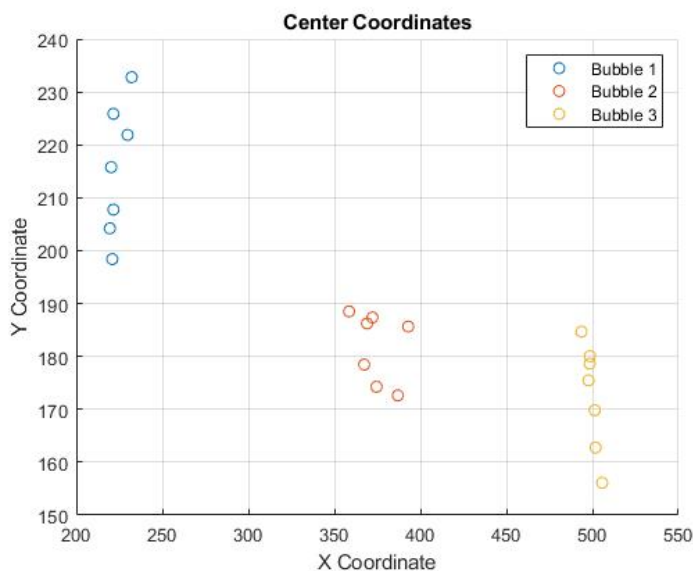

Figure 6. Center coordinates of three carbon dioxide bubbles. Two of the bubbles show vertical movement similar to the air bubble sample, yet the magnitude of movement is almost half. The random movement of Bubble 2 opposes the trend of magnetic field influence.

A third reason for the lack of influence from the magnetic field is the diamagnetic

property of carbon dioxide. Effects of the magnetic field may have been observed in the solution

itself, but the comparative influence with another dissolved gas is currently not available.

Indication that the effect of a magnetic field is plausible is our measurement of significant

movement with the air sample. The air example would contain dissolved oxygen, which is a

paramagnetic gas. Oxygen bubbles would move in the presence of the magnetic field.

3.3 Genetic algorithm

A genetic algorithm is programmed and used to streamline and optimize the analysis of large amounts of data. Our program, created in Matlab, follows the basic guidelines for genetic algorithms (Figure 7). Before the process begins, boundary conditions are set. The borders of bubbles are located by scanning the image rows and columns pixel by pixel, comparing each color value in the image to a specified threshold. Image intensity thresholds are adjusted to prevent particulates or scratches from influencing the bubble recognition image processing. The pixels of the bubbles are recorded and marked as "points of interest". Each point of interest serves to guide the genetic algorithm in finding bubbles.
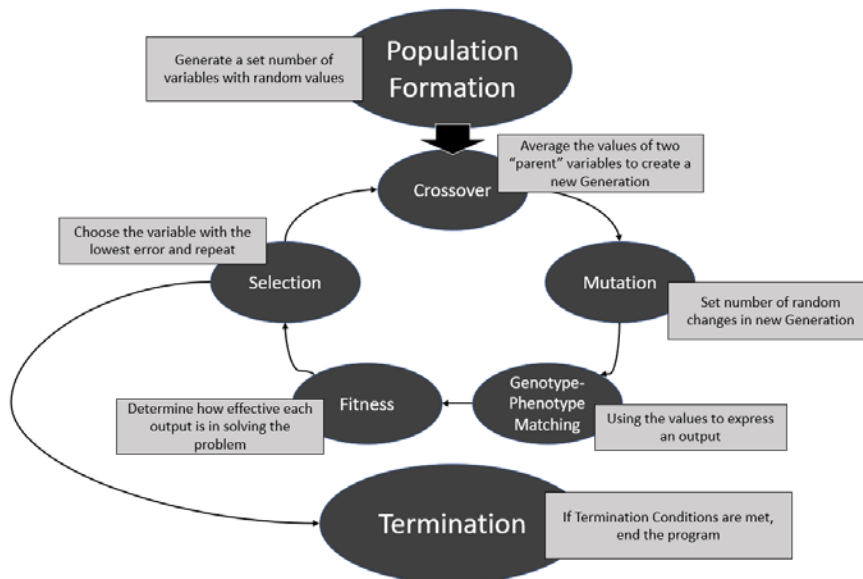

Figure 7. Summary of the flow of a genetic algorithm. Our genetic algorithm requires manual inputs of the number of bubbles present in a sample as well as threshold in order to prevent the inaccurate generation of variables attempting to encompass multiple bubbles.

The initial population randomly generates coordinates and radii for each bubble present in the sample and is bound by the dimensions of the image. Slightly diverging from the basic method, this random population is plot onto a copy of the image to display the progress of the genetic algorithm to the observer, jumping into the Genotype-Phenotype Matching step. The initial population is evaluated for its Fitness by comparing each variable's distance from the points of interest. The Fitness function further is evaluated by the variable's distance from other

15

variables of its designated bubble family, whether it is tracking the first, second, third, etc. bubble, and determined their center coordinates and radii to create a circle. The initial population is sorted from least to greatest error. The termination condition is set to 30 generations, and the "evolution" cycles began.

Our genetic algorithm separated the loop into three functions: Selection, Crossover, Mutation; Genotype-Phenotype Matching; and Fitness. In the first function, the previous generation is sorted from least to greatest error, and the minimum error variable is singled out. This variable is crossed with every other variable and averaged to create a new population. Values within the new population are randomized to prevent the algorithm from consolidating around a local minimum error rather than the absolute minimum error, the bubble itself. The second function displays the values from the previous function as points on the image. The displayed image is updated every generation so the observer can monitor the progress and effectiveness of the genetic algorithm. This overlay is saved for future reference.

The final function evaluates the effectiveness of each variable compared to the points of interest. Every variable is associated with the equation for a circle: $x^2+y^2+r^2=0$. Error is determined by how far from point of interest is to the a coordinate on the sphere with radius r and center (x,y). Every function is called 30 times before the program is terminated.

While the genetic algorithm is able to recognize bubbles in ideal setups, small changes in the experiment caused large scale inaccuracies in the program. Two major errors are present in the algorithm: bubble proximity and circle formation. In the case of bubble proximity, two or more bubbles that are either too close to distinguish or at a certain distance equal to the radius confused the program into locating false bubbles (Figure 8). When presented with multiple points of interest that do not match the algorithm's generated bubble outline, the algorithm will place the outline as a line-of-best-fit. On rare occasions, errors in bubble proximity could be fixed by adjusting the threshold value to better mark points of interest separating the bubbles.
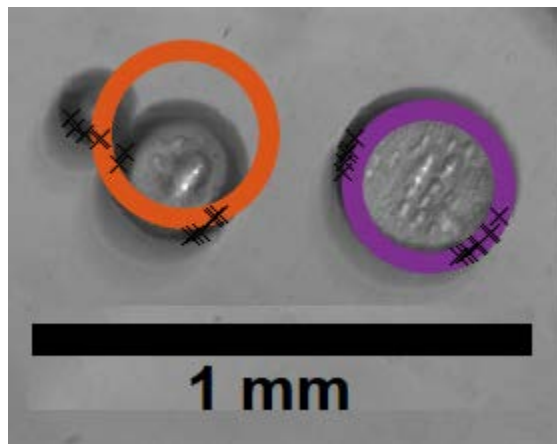

Figure 8. Faulty bubble recognition of the algorithm. As shown, the bubble on the far right is easily identified due to its isolation in the sample. The two bubbles on the left are incorrectly identified as one bubble, with the program outline placing itself between certain points of interest. Note that the threshold is too low to mark the other side of the bubbles, as bubbles lower in the well slide appeared out of focus compared to bubbles that were closer to the surface.

In the case of the circle formation, the qualifying equation for the Fitness function often does not match every bubble generated. If a bubble is captured between two frames of the image, the stitched image produces an elliptical bubble that the algorithm does not recognize (Figure 9). This indicates a problem with the genetic algorithm "initiation" process that determines the Points of Interest.
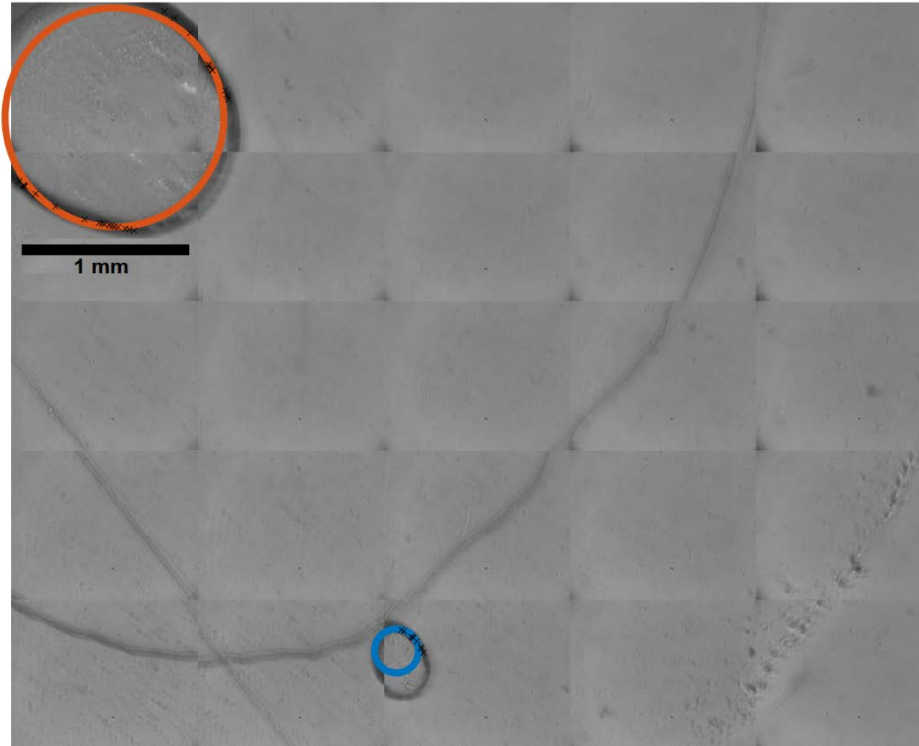
Figure 9. Incorrect bubble recognition due to image capture issues. The blue bubble drifted upwards and was caught between frames. The resulting outline is unable to capture the bubble accurately. Furthermore, the orange bubble in the top left is not entirely in-frame, and the remaining points of interest can influence the other outlines.

Bubbles that touch the surface of the slide deform into an elliptical shape that the genetic algorithm does not recognize. Bubbles that are partially out of frame are not properly identified, yet their points of interest remain in the algorithm calculations. When bubbles are not accurately located, their points of interests continue to influence the surrounding bubble outlines. This factor may sabotage the entire sample due to the algorithm's programming (Figure 10). A suggested solution is to outline the bubbles based solely on threshold without relying on the circle equation. Radius could thereby be calculated through point proximity. However, such a method does not solve bubble proximity, and it may treat an incorrectly captured bubble as two bubbles.
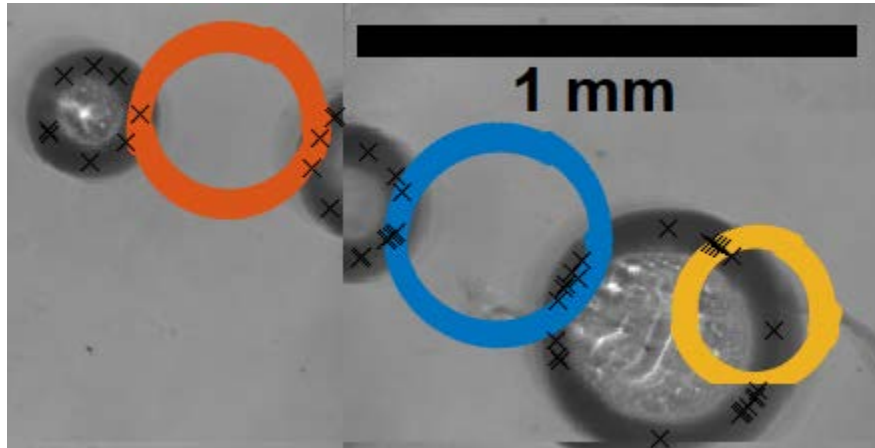
Figure 10. Inaccurate bubble location influencing the surrounding bubble recognition. Due to a sudden movement during the image capture cycle, the central bubble was split. The algorithm recorded its points of interest, and those points caused the program to create bubble guides between two real bubbles.

Conclusion

We measure the formation and volume growth of microbubbles in both water and gold nanoparticle solution under magnetic and non-magnetic conditions. We find that the volume growth rate of bubbles depended on the initial size of the bubble. We showed that greater numbers of bubbles possessed smaller radii as compared to single bubble samples. Carbon dioxide bubbles showed no significant motion under a magnetic field, and the motion of air bubbles was inconsistent. The lack of influence of the magnetic field is attributed to the low strength LED light used in place of a stronger continuous wave illumination and low number of samples, lack of experiments with oxygen, and challenges posed with the genetic algorithm. The genetic algorithm used to examine and identify bubbles was successful for most of the samples, and its errors and shortcomings are presented.

References

Anderson, L. J., Hansen, E., Lukianova-Hleb, E. Y., Hafner, J. H., & Lapotko, D. O. (2010). Optically guided controlled release from liposomes with tunable plasmonic nanobubbles. *Journal of Controlled Release*, *144*(2), 151-158.

Baffou, G., Polleux, J., Rigneault, H., & Monneret, S. (2014). Super-heating and micro-bubble generation around plasmonic nanoparticles under cw illumination. *The Journal of Physical Chemistry C*, *118*(9), 4890-4898.

Chen, H., & Hwang, J. H. (2013). Ultrasound-targeted microbubble destruction for chemotherapeutic drug delivery to solid tumors. *Journal of therapeutic ultrasound*, *1*(1), 10.

Hsieh, T. H., & Keh, H. J. (2012). Motion of a colloidal sphere with interfacial self-electrochemical reactions induced by a magnetic field. *The Journal of chemical physics*, *136*(17), 174702.

Kim, H. K., Hanson, G. W., & Geller, D. A. (2013). Are gold clusters in RF fields hot or not?. *Science*, *340*(6131), 441-442.

Kramer, O. (2017). *Genetic algorithm essentials* (Vol. 679). Springer.

Liang, J., Liu, H., Yu, J., Zhou, L., & Zhu, J. (2019). Plasmon-enhanced solar vapor generation, *Nanophotonics*, *8*(5), 771-786.

Lukianova-Hleb, E., Hu, Y., Latterini, L., Tarpani, L., Lee, S., Drezek, R. A., ... & Lapotko, D. O. (2010). Plasmonic nanobubbles as transient vapor nanobubbles generated around plasmonic nanoparticles. *ACS nano*, *4*(4), 2109-2123.

Mandracchia, B., Wang, Z., Ferraro, V., Villone, M. M., Di Maio, E., Maffettone, P. L., & Ferraro, P. (2019). Quantitative imaging of the complexity in liquid bubbles'

evolution reveals the dynamics of film retraction. *Light: Science & Applications*, *8*(1), 1-12.

Metwally, K., Mensah, S., & Baffou, G. (2015). Fluence threshold for photothermal bubble generation using plasmonic nanoparticles. *The Journal of Physical Chemistry C*, *119*(51), 28586-28596.

Neumann, O., Urban, A. S., Day, J., Lal, S., Nordlander, P., & Halas, N. J. (2013). Solar vapor generation enabled by nanoparticles. *ACS nano*, *7*(1), 42-49.

Wang, K., Pei, P., Pei, Y., Ma, Z., Xu, H., & Chen, D. (2016). Magnetic field induced motion behavior of gas bubbles in liquid. *Scientific reports*, *6*(1), 1-6.

Wang, Y., Zaytsev, M. E., The, H. L., Eijkel, J. C., Zandvliet, H. J., Zhang, X., & Lohse, D. (2017). Vapor and gas-bubble growth dynamics around laser-irradiated, water-immersed plasmonic nanoparticles. *ACS nano*, *11*(2), 2045-2051.

Wang, Z., Horseman, T., Straub, A. P., Yip, N. Y., Li, D., Elimelech, M., & Lin, S. (2019). Pathways and challenges for efficient solar-thermal desalination. *Science advances*, *5*(7), eaax0763.